Research Square

Preprints are preliminary reports that have not undergone peer review.
They should not be considered conclusive, used to inform clinical practice,
or referenced by the media as validated information.

Mobility-Based Target Selection and Preliminary Humic-Fraction Screening for Pb/Cd Removal from Smelting-Slag-Impacted Waters

Haiqing Yang
Hohai University
Zhixiao Mao
zhixiaomaomail@163.com

Southwest University of Science and Technology
Qiming Wang
Southwest University of Science and Technology
Yong Zhen
Kunming Engineering Corporation Limited
Bixia Yuan
Kunming Engineering Corporation Limited
Yaoyao Shen
Chengdu Engineering Corporation Limited

Research Article

Keywords: smelting slag, leaching, Pb, Cd, humic acid, humin, water treatment, adsorption, heavy-metal removal

Posted Date: November 20th, 2026

DOI: https://doi.org/10.21203/rs.3.rs-10930338/v1

License: This work is licensed under a Creative Commons Attribution 4.0 International License.
Read Full License

Mobility-Based Target Selection and Preliminary Humic-Fraction Screening for Pb/Cd Removal from Smelting-Slag-Impacted Waters

Haiqing Yang[a,b], Zhixiao Mao[c,d,*], Qiming Wang[c,d], Yong Zhen[b], Bixia Yuan[b], Yaoyao Shen[b]

[a]College of Agricultural Science and Engineering, Hohai University, Nanjing 211100, China

[b]Kunming Engineering Corporation Limited, Kunming 650051, China

[c]School of Environment and Resource, Southwest University of Science and Technology, Mianyang, Sichuan 621010, China

[d]Low-cost Wastewater Treatment Technology International Sci-Tech Cooperation Base of Sichuan Province, Mianyang, Sichuan 621010, China

*Corresponding author: Zhixiao Mao. E-mail: zhixiaomaomail@163.com

ABSTRACT

Metal-bearing drainage from smelting-slag stockpiles requires identification of mobile contaminants before removal options can be selected. We linked source-term assessment of a lead–zinc slag stockpile with preliminary batch screening of site-derived humic fractions for Pb^{2+} and Cd^{2+} removal. Slag from four stockpile locations (Z1–Z4) was characterized by SEM–EDS and XRD, and bulk inventories were compared with standardized acid-leaching behavior. Cd release reached 36.37–44.14 mg L^{-1} under HJ/T 299 conditions and exceeded the regulatory limit by more than 36-fold, whereas Pb release remained comparatively low. Cd was therefore the principal mobile target under the applied test. Downstream Cd/Zn enrichment at surface-water sites W5–W6 and a groundwater anomaly at U2 provided field context for localized industrial influence, without proving a unique source. HA and HM were then compared in controlled single-metal nitrate solutions. Apparent removal was defined from

dissolved-metal concentrations after 0.45 μm filtration. At 25 °C, fitted Langmuir capacities for HA were 8.97 mg g^{-1} for Pb^{2+} and 6.47 mg g^{-1} for Cd^{2+}; HA also showed faster uptake than HM. Pseudo-second-order and Freundlich fits supported comparative screening, while elemental, UV–Vis, SEM and FTIR data provided supporting evidence for differences in site accessibility. Unlike studies that directly treat real metallurgical wastewater or evaluate long-term dynamic leaching, this work uses a linked source-screening design to prioritize the next treatment tests. The resulting workflow is therefore a bounded basis for mobility-based target selection and humic-sorbent screening, not validation of a real-wastewater or flow-through process.

Keywords: smelting slag; leaching; Pb; Cd; humic acid; humin; water treatment; adsorption; heavy-metal removal

1. Introduction

Industrial development has generated large quantities of metallurgical residues (e.g., tailings and smelting slags) that are commonly stored or disposed without rigorous stabilization, creating long-lived geochemical sources of metal(loid)s to the near-surface environment(Chen et al., 2024a; Xu et al., 2021). In particular, lead–zinc production generates substantial amounts of smelting slag(Ma et al., 2023); approximately 0.7 t of slag can be produced per ton of lead, and ~0.96 t per ton of zinc(Zhou et al., 2025). These slags typically contain elevated concentrations of heavy metals and are therefore of environmental concern(Tao et al., 2019). Where residues

47 are stored in open-air stockpiles due to technological and economic constraints(Piatak
48 et al., 2015), low-temperature weathering and episodic rainfall infiltration can promote
49 dissolution, desorption, and physical dispersion of metal-bearing phases (Luo et al.,
50 2024; Zeng et al., 2023). Such stockpiles therefore have the potential to behave as
51 persistent secondary sources to surrounding soil–water systems over decadal
52 timescales(Hu et al., 2025).

53 Field investigations in industrial and mining-impacted regions have repeatedly
54 reported metal accumulation in adjacent soils and contamination of water
55 bodies(Moghimi Dehkordi et al., 2024), indicating limited natural attenuation and
56 persistent source loading(Rodríguez et al., 2009; Srinivasa Gowd et al., 2010). In slag-
57 affected settings, open stockpiles contain large metal inventories and remain exposed
58 for long periods(Peng et al., 2022). Metals can reach receiving waters through runoff,
59 particle dispersion, and subsurface seepage(Lin et al., 2018), producing variable
60 influent composition and complicating treatment-target selection(A. Wang et al., 2024).
61 Because complete removal or engineered containment of large slag piles is often
62 constrained by cost and logistics(Mohammadi et al., 2020), water-risk management
63 requires both source control and physicochemical processes that reduce dissolved-
64 metal concentrations(Shu and Sasaki, 2022; Zhou et al., 2024). Identifying the metals
65 that are readily leached is therefore essential before selecting adsorption-based
66 treatment or immobilization strategies.

67 The treatability of slag-derived metals depends not only on bulk inventory but also

on aqueous speciation and partitioning to reactive solid phases(Guo et al., 2026; Klučáková and Enev, 2024). Humic substances (HS), a major component of soil organic matter, are typically negatively charged and contain abundant reactive functional groups. These properties enable metal removal from water through electrostatic attraction, ion exchange, and coordination(Tan et al., 2019). Although humic materials have complex molecular architectures(Ding et al., 2019), they are commonly conceptualized as polyphenol- and quinone-derived frameworks bearing diverse functional moieties (Figure S1)(Tandy et al., 2004). Their weak acidity and pH-dependent deprotonation regulate metal partitioning between aqueous and solid phases(Z. Wang et al., 2024). Previous studies have shown that humic fractions with different molecular characteristics exhibit distinct complexation behavior toward Cd and Zn, and that higher aromaticity can enhance binding strength(He et al., 2016). Pb adsorption may also increase with pH because proton competition decreases and more binding sites become deprotonated(Xiong et al., 2013). Carboxyl and phenolic groups are frequently identified as important metal-binding sites(Qu et al., 2022). Clarifying these interactions under contamination-relevant conditions can therefore support the design of low-cost sorption and immobilization steps for metal-bearing waters(Chen et al., 2024b; Pan et al., 2023).

Humic substances are operationally classified by solubility into humic acid (HA), fulvic acid (FA), and humin (HM). HA and HM contain C, H, O, N, and S, and their structural characteristics are commonly assessed using atomic ratios such as H/C and

O/C(Ma et al., 2025). HA is soluble under alkaline conditions, whereas HM is largely insoluble and commonly contains stronger organo–mineral associations, higher ash contents, and more heterogeneous aliphatic or polysaccharide-like components(Kögel-Knabner, 2017). Total oxygen content alone does not define metal-binding performance because the accessibility and chemical environment of potential sites also matter. HA–metal interactions have been widely studied, but HM adsorption and its relative contribution to metal immobilization remain less constrained in slag-affected settings(Lu et al., 2023; Wang et al., 2025).

Spectroscopic studies indicate that oxygen-containing groups in HA, including carboxyl and hydroxyl groups, can participate in metal binding, while infrared shifts record changes in bonding environments after uptake(Cui et al., 2022; Subdiaga et al., 2019). HM may also provide binding sites through oxygen-containing moieties and organo–mineral structures, but its insolubility and heterogeneous composition complicate direct comparison(Tang et al., 2014). Comparing HA and HM in controlled single-metal solutions can therefore provide preliminary evidence for sorbent selection. Such screening does not show that either raw fraction is already a deployable treatment material.

The study addressed a decision problem that is often separated into two modules: which metals released from a smelting-slag source should be prioritized for aqueous treatment, and which locally available humic fraction is the more defensible candidate for follow-up removal tests. We therefore linked three steps: source characterization

and standardized leaching, comparison of HA and HM for dissolved Pb^{2+} and Cd^{2+} removal, and interpretation of operating and material observations for sorbent selection. Slag from four stockpile locations (Z1–Z4) was characterized by SEM–EDS, XRD and standardized leaching, whereas HA and HM were compared in controlled single-metal batch systems using pH, contact-time, equilibrium and complementary characterization data. Unlike dynamic-column leaching studies, pretreatment studies and real-wastewater treatment studies, the present design does not claim long-term source attenuation or direct treatment performance. Its contribution is narrower and more operational: it establishes an evidence-bounded priority order for the next treatment experiments by connecting source mobility to preliminary sorbent choice.

2. Materials and experimental methods

2.1. The preparation of materials

2.1.1. Site setting and hydrochemical monitoring

Surface water and groundwater monitoring were conducted to characterize the background hydrochemical conditions of the study area and to support environmental risk assessment of slag stockpiles. The study area is situated in the southwestern region of Sichuan Province, characterized by a mountainous terrain under a subtropical monsoon climate. Precipitation is concentrated in the summer months, and the terrain exhibits complex diversity dominated by north-south trending mountain ranges. Within the study area lies an industrial park housing metal recycling and smelting facilities,

130 electronics manufacturing plants, and other enterprises. These industries are engaged in
131 the year-round processing of lead–zinc-containing slags and related waste materials.
132 Most processed smelting slags are typically stored in open-air stockpiles after minimal
133 treatment.

134 Based on the local topography and the operational conditions of the slag storage
135 site, surface water samples were collected from areas surrounding a lead-zinc smelting
136 waste residue stockpile within an industrial park. The distribution of sampling points
137 and other relevant information is shown in **Fig. 1**.

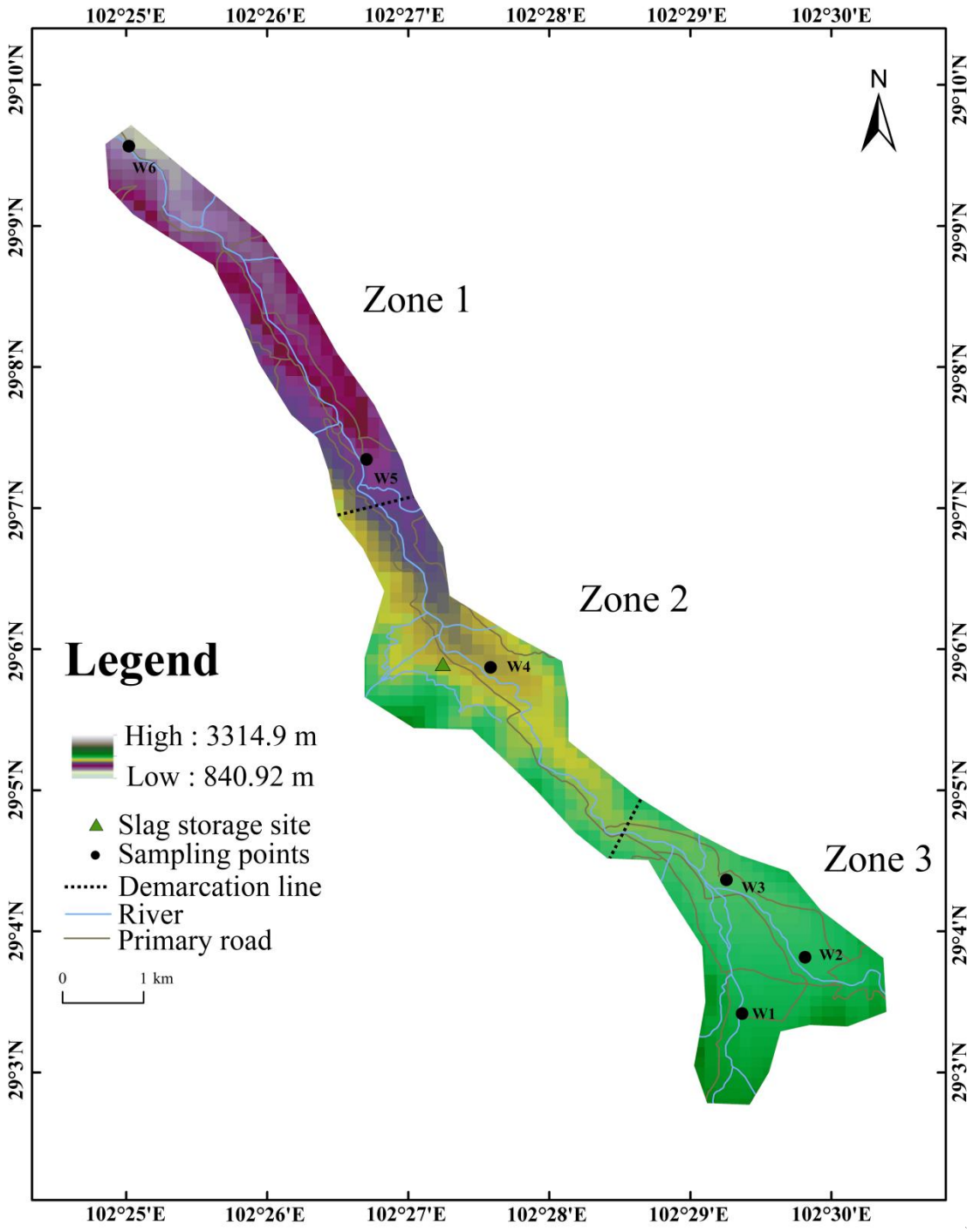


Fig. 1. Spatial distribution of surface-water monitoring sites W1–W6 across Zones 1–3 surrounding the lead–zinc smelting slag stockpile; the network defines the receiving-water context for treatment-target assessment.

The industrial park is situated within an elongated valley terrain, where elevation gradually increases from 900 m in the north to 3,300 m in the south. Based on elevation gradients and functional zoning, the area was divided into three sampling zones: 1)

Zone 1 (900–1,500 m): Primarily residential areas and villages. 2) Zone 2 (1,500–1,900 m): Hosts mineral processing plants, smelters, electronics factories, and lead-zinc slag stockpiles. 3) Zone 3 (1,900–3,300 m): Higher-altitude regions with minimal industrial activity and anthropogenic influence.

The surface runoff system traverses the industrial park and converges toward downstream urban areas. Six surface-water monitoring points were sampled during six monitoring campaigns, with two campaigns conducted each year. Sampling, preservation, and analytical procedures followed the methods summarized in Table S1. Site-level summary values are reported in Table S7, whereas campaign-specific temporal profiles are shown in Figure S2.

Four groundwater monitoring points were established within the study area (Fig. 2). One point was located upstream of the industrial park, two were near slag stockpiles, and one was at the downstream exit of the park. The wells were monitored during six campaigns, with two campaigns conducted each year. Sampling-point configurations are summarized in Table S2, the site-level summary results are provided in Table S8, and the applicable analytical criteria are provided in Table S3.

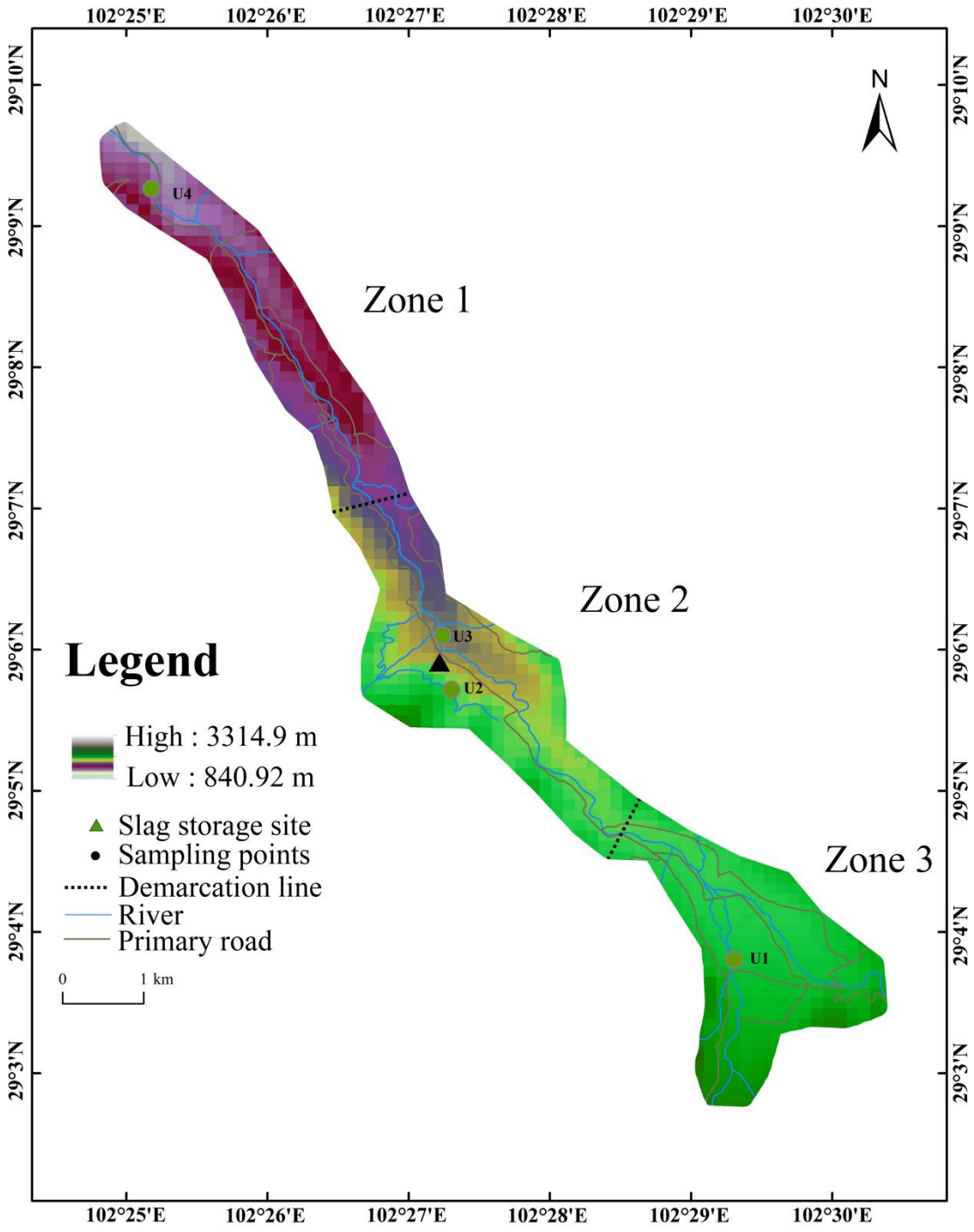


Fig. 2. Spatial distribution of groundwater monitoring wells U1–U4, including upstream, near-stockpile, and downstream locations used to define the field context for dissolved-metal control.

2.1.2. Sampling of waste residue specimens

Slag samples from the stockpile areas were randomly collected following the Technical Specifications for Sampling and Sample Preparation of Industrial Solid

Waste (HJ/T20-1998). Surface residues were excavated to obtain representative composite samples, with detailed documentation of sampling categories, morphological characteristics, geographic coordinates (latitude/longitude), and elevation. To minimize moisture interference, air was evacuated from sample bags prior to hermetic sealing for preservation.

2.1.3. Extraction of humic substances

Soil samples were collected from areas adjacent to the slag stockpile for the extraction of humic fractions. In parallel, slag (waste residue) samples were collected directly from the slag pile and classified into four representative samples (Z1–Z4), corresponding to four sampling points within the stockpile, for subsequent characterization and leaching assessments (Section 2.3). During sampling, multiple subsamples were composited, visible stones and plant debris were removed, and the homogenized material was quartered to obtain representative subsamples. All samples were placed in sealed bags, and air was expelled as much as possible prior to sealing to minimize moisture interference during storage and transport. The major analytical instruments used in this study are listed in Table S4. Humic acid (HA) and humin (HM) were extracted and purified from soil humus using the method recommended by the International Humic Substances Society (IHSS)(Thurman and Malcolm, 1981).

2.2. Treatment-oriented batch experiments for aqueous Pb/Cd removal

2.2.1. General batch removal procedure

Preliminary batch screening was conducted using humic acid (HA) and humin (HM) extracted from soils near the slag stockpile. Unless otherwise stated, 20 mg of HA or HM was added to 20 mL of a single-metal nitrate solution in capped conical flasks, giving a solid-to-liquid ratio of 1.0 g L^{-1}. $Cd(NO_3)_2$ and $Pb(NO_3)_2$ stock solutions were prepared in ultrapure water and diluted to the concentrations specified for each experiment. Initial pH was adjusted with dilute HNO_3 or NaOH, and suspensions were mixed in a thermostatic shaker. After contact, suspensions were allowed to stand briefly and filtered through 0.45 μm membranes. Pb^{2+} and Cd^{2+} concentrations in the filtrates were measured by ICP-OES. Apparent removal and uptake are operationally defined by the concentration decrease measured after this filtration step. They may include sorption together with any contribution from hydrolysis, colloid retention, membrane adsorption, or incipient precipitation. The tests therefore provide controlled comparative screening rather than treatment performance in field water or wastewater. Each ICP-OES analytical sequence included a calibration blank, a zero standard, and multi-point calibration standards at 0.1, 0.2, 1, 2, 10, and 20 mg L^{-1}. Concentrations below the method detection limit were reported as ND; blank-corrected negative instrument responses were also treated as below-detection results and were not interpreted as negative concentrations. The analytical method detection and

quantification limits were 0.03 and 0.10 mg L^{-1} for Pb, and 0.02 and 0.07 mg L^{-1} for Cd, respectively. Measured recoveries were 98% for Pb and 97% for Cd.

All batch experiments were performed in triplicate, and procedural blanks without sorbent were included. For datasets retaining independent replicate values, results were summarized as the mean ± sample standard deviation (SD; n = 3, denominator n − 1). Kinetic and isotherm fitting parameters were treated as point estimates; SD values were not reconstructed from fitted or single-reported values. Operationally defined apparent uptake was calculated by mass balance according to Eq. (1):

$$q_t = (C_0 - C_t)\, V/\mathrm{m} \quad (1)$$

where q_t(mg·g^{-1}) is the adsorption capacity at time t, $C_0$and C_t(mg·L^{-1}) are the initial and time-dependent concentrations, respectively, V(L) is the solution volume, and m(g) is the sorbent mass. At equilibrium, $q_e$was calculated by replacing $C_t$with C_e.

2.2.2. pH and temperature effects on aqueous removal

To investigate the effects of pH and temperature on Pb^{2+} and Cd^{2+} adsorption, the initial pH of the metal solutions was adjusted to 2.00, 3.00, 4.00, 5.00, 6.00, and 7.00 using dilute HNO_3 or NaOH, and adsorption experiments were conducted at 15, 25, and 35 °C under otherwise identical conditions. In both cases, the remaining experimental conditions followed the general adsorption procedure. After adsorption, the suspensions were filtered and analyzed by ICP-OES as described above.

2.2.3. Contact-time and kinetic screening

For kinetic experiments, 20 mg of HA or HM was added to 20 mL of $Cd(NO_3)_2$ solution (initial pH 3.0) at initial concentrations of 10, 20, and 50 $mg \cdot L^{-1}$, and the suspensions were shaken at 150 r min^{-1} and 25 °C. Aliquots were collected at predetermined time intervals (1, 2, 3, 5, 7, 10, 15, 30, 60, 120, 180, and 240 min), allowed to stand briefly, and then filtered through 0.45 μm membranes prior to ICP-OES analysis. Pb^{2+} kinetic experiments were conducted using the same procedure and conditions. The resulting kinetic data for Pb^{2+} and Cd^{2+} adsorption on HA and HM were fitted using pseudo-first-order (PFO) and pseudo-second-order (PSO) models.

Eq. (2) shows the pseudo-first-order model (PFO):

$$\ln(q_e - q_t) = \ln q_e - k_1 t \quad (2)$$

where q_e and q_t ($mg \cdot g^{-1}$) are adsorption capacities at equilibrium and at time t, respectively, and k_1 (min^{-1}) is the PFO rate constant.

Eq. (3) shows the pseudo-second-order model (PSO):

$$t/q_t = 1/(k_2 q_e^2) + t/q_e \quad (3)$$

where k_2 ($g \cdot mg^{-1} \cdot min^{-1}$) is the PSO rate constant.

2.2.4. Equilibrium removal and isotherm screening

For isothermal adsorption experiments, 20 mg of HA or HM was added to 20 mL of $Cd(NO_3)_2$ solution (initial pH 3.0) with initial Cd^{2+} concentrations of 10, 20, 30, 40, and 50 $mg \cdot L^{-1}$. The suspensions were shaken at 25 °C under light-protected conditions to minimize potential alteration of humic fractions. After shaking for 4 h, the mixtures

were further equilibrated for 12 h. The suspensions were then filtered through 0.45 μm membranes and analyzed by ICP-OES. Pb^{2+} isotherm experiments were performed using the same procedure and conditions. The resulting equilibrium adsorption data were subsequently fitted using Freundlich, Langmuir, and Temkin isotherm models.

Eq. (4) shows the Freundlich model:

$$q_e = K_f C_e^{1/\mathrm{n}} \quad (4)$$

where K_f is the Freundlich constant and $n$reflects adsorption heterogeneity.

Eq. (5) shows the Langmuir model:

$$C_e/q_e = 1/(K_L q_m) + C_e/q_m \quad (5)$$

where q_m (mg·g^{-1}) is the maximum adsorption capacity and K_L (L·mg^{-1}) is the Langmuir affinity constant.

Eq. (6) shows the Temkin model:

$$q_e = (RT/\mathrm{b}) \ln(A_T C_e) \quad (6)$$

where R is the universal gas constant (8.314 J·mol^{-1}·K^{-1}), T(K) is temperature, $b$is the Temkin constant related to adsorption heat, and A_T(L·mg^{-1}) is the Temkin isotherm constant.

2.3. Source and sorbent characterization methods

2.3.1. Corrosivity test of slag

The corrosivity of slag was determined using the glass electrode method according

to the Chinese national standard *Solid Waste—Determination of Corrosivity—Glass Electrode Method* (GB/T 15555.12-1995).

2.3.2. Total content analysis of slag

Total metal contents in slag were determined after complete acid digestion. Briefly, slag samples were digested using a mixed acid system (HCl, HNO_3, HF, and $HClO_4$) under elevated temperature to achieve full dissolution. After digestion, the extracts were diluted to a fixed volume with dilute HNO_3, and metal concentrations were quantified by inductively coupled plasma optical emission spectrometry (ICP-OES). The digestion protocol is summarized in **Table S5**.

2.3.3. Leaching toxicity test of slag

Leaching toxicity was evaluated using the standardized sulfuric–nitric acid procedure specified in HJ/T 299-2007 (Technical Specification for Leaching Toxicity of Solid Wastes). This test provides a regulatory screening measure of acid-extractable release and does not reproduce natural rainfall chemistry. A sulfuric–nitric acid mixture (HNO_3:H_2SO_4 = 2:1, w/w) in ultrapure water was used at a liquid-to-solid ratio of 10 L kg^{-1}. Suspensions were oscillated at 110 ± 10 r min^{-1} and 25 ± 2 °C for 8 h, followed by 16 h of settling. Leachates were then collected and analyzed by ICP-OES. Key parameters are listed in Table S6.

2.3.4. Characterization of Soil Humus

Elemental compositions of HA and HM were determined using an elemental analyzer. Appropriate amounts of dried samples were weighed into tin capsules, and C, H, N, and

S contents were measured directly. Oxygen content (O%) was calculated by mass balance according to Eq. (7):

$$O\%=100\%-C\%-H\%-N\%-S\%-Ash\% \quad (7)$$

Ash content was determined gravimetrically after ignition and calculated as Eq. (8):

$$Ash\%=(m_2-m_1)/m \quad (8)$$

where m is the original sample mass (g), m_1 is the mass of the empty crucible (g), and m_2 is the mass of the crucible plus ash residue after ignition (g).

For UV–Vis absorption spectroscopy, 0.2 g of extracted humus was dissolved in a small volume of NaOH solution, the pH of the solution was adjusted to neutral, and the spectrum was recorded over 200–800 nm using a UV–Vis spectrophotometer. Fourier transform infrared (FTIR) spectra were obtained by mixing the dried sample with KBr, grinding the mixture into a fine powder, and pressing it into pellets. Spectra were recorded over the 4000–400 cm^{-1} range with 32 scans per sample to ensure adequate signal-to-noise optimization.

3. Results and discussion

The Results and Discussion follow a source-to-treatment decision sequence. We first use receiving-water context, bulk inventories and standardized leaching to distinguish the metal that is most mobile under the applied test from metals that are abundant but less mobile. That decision then defines the Pb/Cd screening space for HA

and HM, which are compared using contact-time, equilibrium, pH and characterization evidence. The adsorption experiments are controlled single-metal screens and do not reproduce the field waters or validate a full-scale process; their purpose is to rank follow-up candidates within the source-mobility context established in Section 3.1.

3.1. Treatment-target identification from receiving-water context and source mobility

3.1.1. Surface water quality analysis

Surface-water results are summarized at the site level in Table S7, with values below the method detection limit reported as ND. The six campaign-specific temporal profiles are shown in Figure S2. Mean concentrations followed the order Zn > Pb > Cd > Cu > As. Pb, Cu, and As met the Class III criteria at all sites, whereas Zn exceeded the limit at W5 and Cd exceeded it at W5 and W6 (Table S3). Cd and Zn were therefore enriched at downstream relative to upstream locations. Across six campaigns, downstream sites also showed higher Cd/Zn concentrations after runoff passed through the industrial activity zone (Figure S2). This spatial association is consistent with an industrial-area contribution, but the monitoring design does not uniquely attribute the metals to the slag stockpile.

3.1.2. Groundwater quality analysis

Groundwater results show a localized anomaly at U2, where Pb, Cd, and Zn exceeded the Class III limits, while the other wells remained within permissible ranges

(Table S8). Table S8 provides the site-level summary, and U2 had the highest metal concentrations among the four wells across the six campaigns shown in Figure S3. Its proximity to the industrial and stockpile area makes a local contribution plausible. However, the available spatial monitoring cannot distinguish the slag stockpile from other industrial sources or establish a specific transport pathway.

3.1.3. SEM-EDS analysis of slag

SEM images of slag samples are shown in **Figure S4**, and the corresponding EDS composition is summarized in **Table S9**. Representative EDS spectra of the waste residue are provided in **Figure S5**. The slag surface exhibited a rough, clustered morphology composed of tightly packed flaky and layered structures, indicating heterogeneous microtextures. EDS analysis identified C, O, Fe, Pb, S, Si, Al, K, and Ca as major elements (**Table S9**), consistent with a mixture of mineral phases and metal-bearing constituents in the slag matrix.

3.1.4. XRD phase analysis of slag

XRD patterns were analyzed by PDF database matching, and the assigned phases are presented in Figure S6. Diffraction peaks were numerous and partially overlapping. SiO_2, metal oxides, sulfates, and phosphates were tentatively identified, while several reflections could not be assigned conclusively. The patterns therefore indicate a compositionally heterogeneous mixture containing crystalline and potentially poorly crystalline components. The contribution of individual phases to metal release was not resolved by the present measurements.

3.1.5. Corrosivity test of slag

Corrosivity analysis was conducted on slag samples with parallel replicates, and pH was measured using a calibrated meter (Fig. 3). The mean slag pH was 5.68. All measured values met the non-corrosive criterion under the applied standard (Table 1). This solid-sample pH measurement is distinct from the chemical conditions used in the HJ/T 299 leaching test.

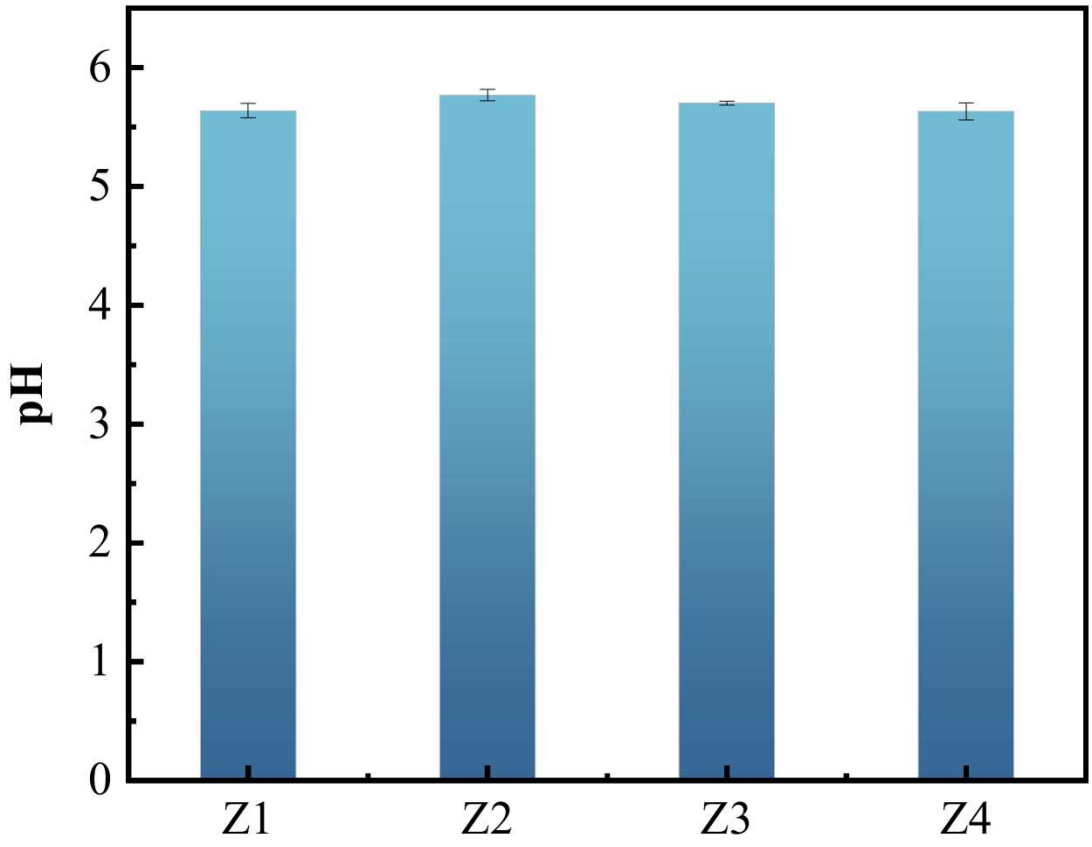


Fig. 3. pH of smelting slag collected at four stockpile sampling points (Z1–Z4), measured in parallel replicates as a source-condition indicator relevant to acid-leaching and treatment-target assessment.

3.1.6. Total heavy metal content in slag

Total metal contents show a substantial inventory in the stockpile (Figs. 4–5). Pb and Zn concentrations were 5,460–7,916 and 14,606–18,215 mg kg^{-1}, respectively, while Cd concentrations were 91.9–197 mg kg^{-1}. Similar distributions across Z1–Z4

indicate compositional consistency among the sampled locations, although the cause of that pattern was not tested. Together with standardized leaching and nearby water anomalies, these measurements identify the stockpile as a plausible metal source. They do not establish its proportional contribution relative to other industrial sources.

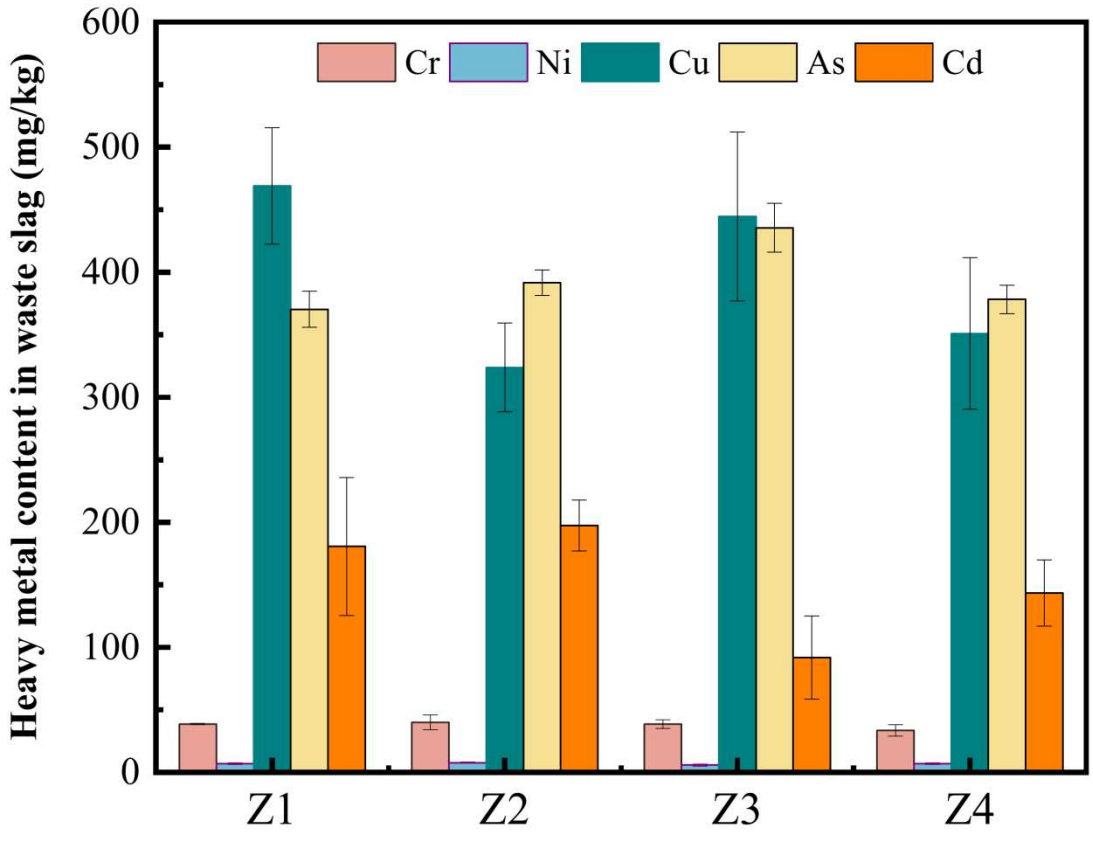


Fig. 4. Total concentrations of selected metals in slag samples from four stockpile points (Z1–Z4), showing bulk inventories that are compared with aqueous mobility before treatment screening.

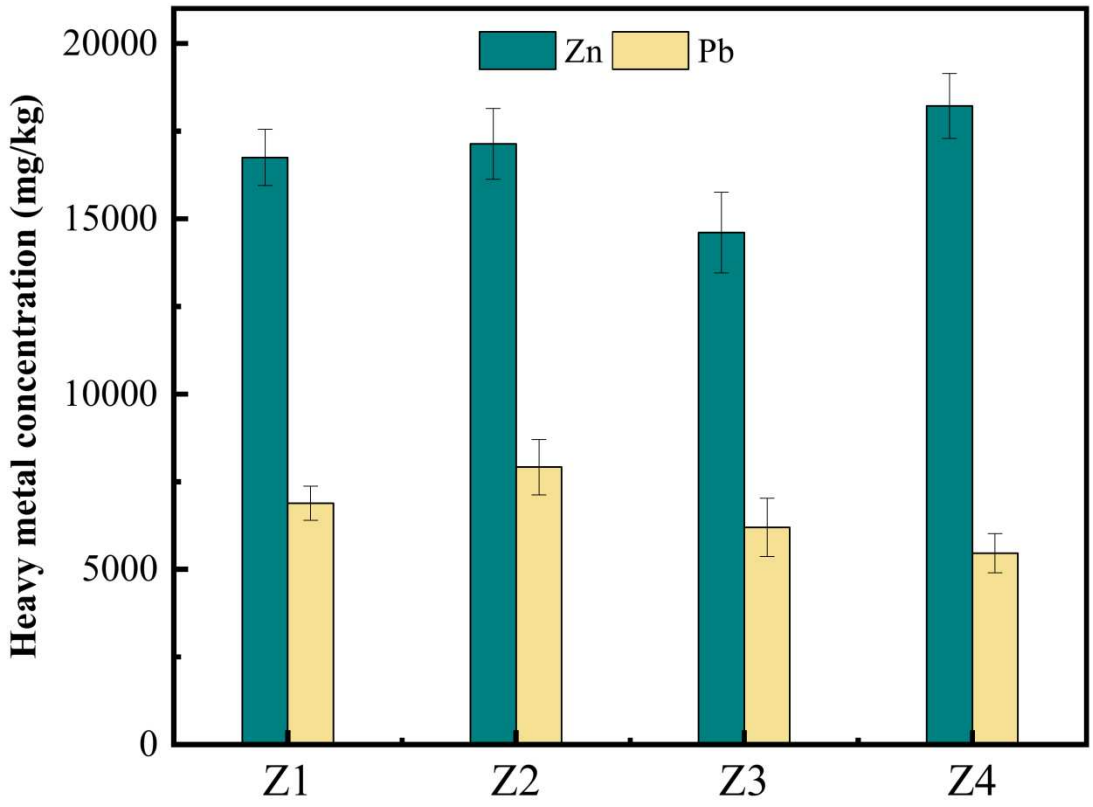


Fig. 5. Total concentrations of Pb and Zn in slag samples from four stockpile points (Z1–Z4), providing inventory context for selecting metals for aqueous-removal screening.

3.1.7. Leaching toxicity of slag

As shown in Fig. 6, standardized acid leaching separated the source inventory from the mobile treatment target. Cd reached 36.37–44.14 mg L^{-1} and exceeded the 1 mg L^{-1} regulatory limit, whereas Pb remained below its limit despite its high bulk inventory (Table 1). Cd was therefore prioritized for aqueous-removal development, while Pb remained relevant as a high-inventory co-contaminant. This contrast supports mobility-based target selection. The HJ/T 299 result is a regulatory screening signal, not a prediction of natural-rainfall concentrations.

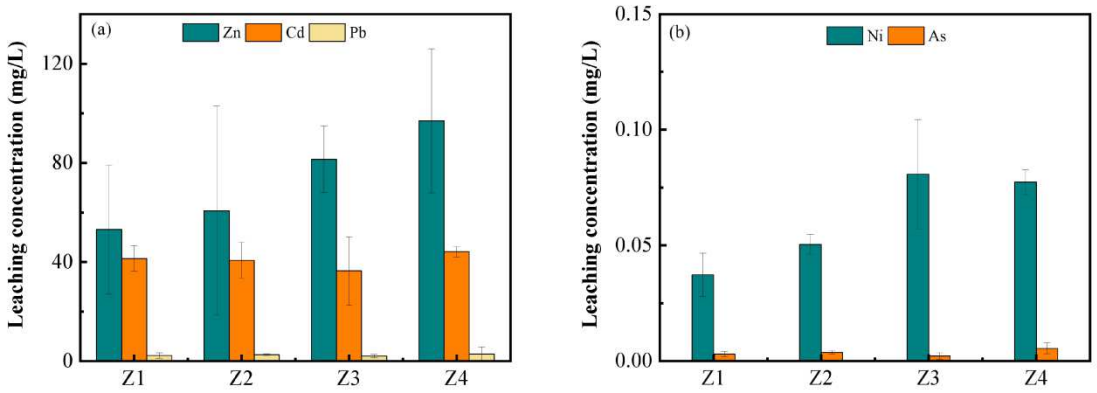


Fig. 6. Standardized acid-leaching concentrations from slag samples: (a) Zn, Cd, and Pb; (b) Ni and As. The leaching profile is used to identify mobile treatment targets under HJ/T 299 conditions.

Table 1 Regulatory limits used for leaching-toxicity identification (mg L^{-1}).

No.	Element (as total)	Maximum allowable leaching concentration
1	Zinc (Zn)	100
2	Cadmium (Cd)	1
3	Lead (Pb)	5
4	Nickel (Ni)	5
5	Arsenic (As)	5

3.2. Preliminary Pb/Cd removal screening with humic fractions

3.2.1. Concentration effects and adsorption kinetics

The contact-time profiles in Fig. 7 provide the first treatment-screening criterion: how quickly a humic fraction can lower dissolved-metal concentrations under controlled mixing. Pb^{2+} and Cd^{2+} uptake by HA and HM increased rapidly during the first 30 min, when concentration gradients were high and binding sites were available, and then approached a slower regime as sites became occupied. Higher initial

concentrations increased the mass removed per unit mass of both fractions. These data support comparative contact-time selection, but they do not establish the residence time required in a continuous treatment unit.

Table 2 Kinetic-model fitting parameters for apparent Pb^{2+} and Cd^{2+} uptake by HA and HM.

Sample	Initial conc. (mg/L)	Pseudo-first-order model			Pseudo-second-order model			
		k_1	q_e	R^2	k_2	q_e	R^2	h_0
HM+Cd^{2+}	10	0.53	0.44	0.89	0.89	0.48	0.90	0.21
	20	0.41	1.52	0.83	0.41	1.62	0.97	1.08
	50	0.25	3.30	0.86	0.11	3.54	0.97	1.38
HA+Cd^{2+}	10	0.14	0.57	0.91	0.35	0.61	0.96	0.13
	20	0.63	2.19	0.90	0.30	2.32	0.95	1.88
	50	0.51	3.88	0.93	0.21	4.08	0.98	3.5
HM+Pb^{2+}	10	0.36	1.87	0.81	0.31	1.98	0.90	1.22
	20	0.84	4.17	0.87	0.38	4.33	0.98	7.12
	50	0.89	6.25	0.92	0.26	6.49	0.94	10.95
HA+Pb^{2+}	10	1.01	3.99	0.80	0.49	4.13	0.96	8.36
	20	1.07	5.63	0.87	0.40	5.89	0.94	13.88
	50	1.09	7.43	0.81	0.30	7.68	0.98	17.69

Kinetic fitting results are summarized in Table 2. The pseudo-second-order expression generally gave higher R^2 values than the pseudo-first-order expression, and

the fitted initial-rate parameter was higher for HA than HM. These results support HA as the more kinetically responsive fraction in this screening comparison. In contrast to dynamic-column studies that quantify release over long leaching periods, these batch profiles describe sorbent response over laboratory contact time. The fits are empirical and do not identify a unique rate-limiting step or molecular mechanism.

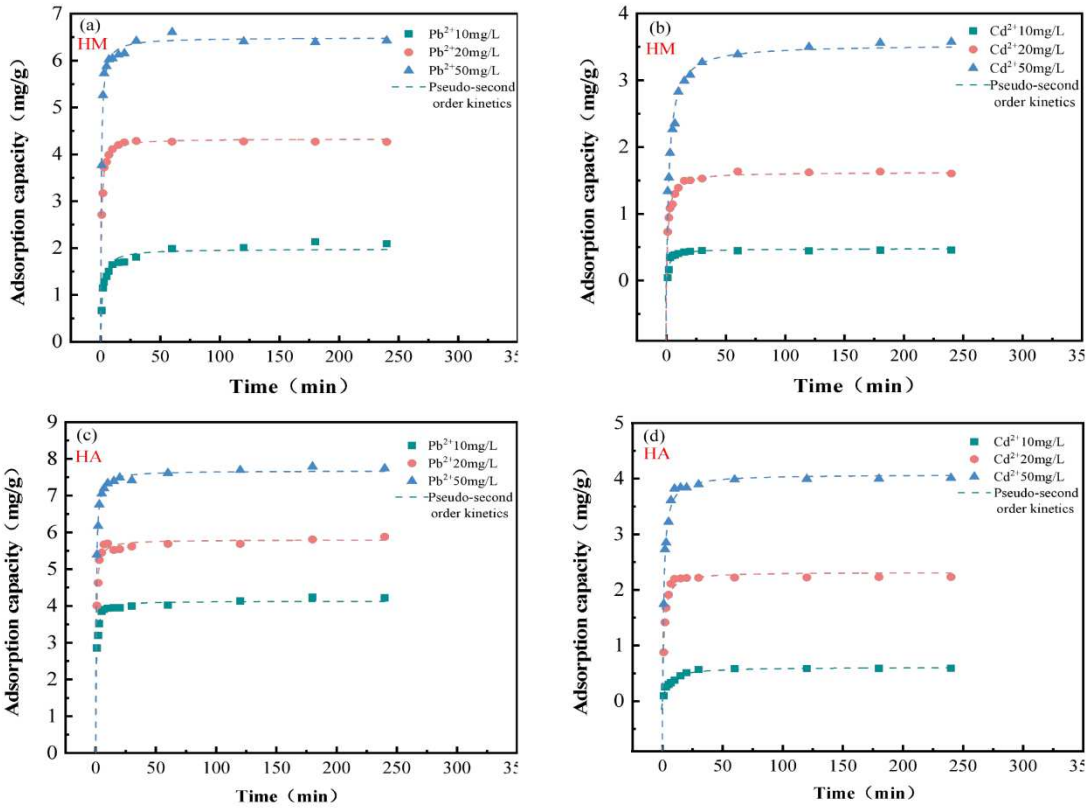


Fig. 7. Contact-time profiles for apparent Pb^{2+} and Cd^{2+} removal by humin (HM) and humic acid (HA): (a) HM–Pb^{2+}, (b) HM–Cd^{2+}, (c) HA–Pb^{2+}, and (d) HA–Cd^{2+}. Experiments were conducted at 150 r min^{-1} and 25 °C in single-metal solutions.

3.2.2. Equilibrium removal and isotherm-based sorbent comparison

Table 3 Isotherm-model fitting parameters for apparent Pb^{2+} and Cd^{2+} uptake by HA and HM.

Sample	Temp. (°C)	Freundlich model			Langmuir model			Temkin model		
		ln K_f	1/n	R^2	b	q_{max}	R^2	A	Kt	R^2
HA+Pb^{2+}	25 ℃	0.92	0.30	0.9889	7.31	8.97	0.9002	1.81	1.73	0.9559
HA+Cd^{2+}		0.25	0.37	0.9802	11.66	6.47	0.9209	1.41	0.88	0.9563
HM+Pb^{2+}		0.34	0.41	0.9789	14.27	8.68	0.9878	2.00	0.61	0.9847
HM+Cd^{2+}		0.19	0.33	0.9989	9.99	5.14	0.9727	1.10	1.07	0.9943

Table footnote: Kf, empirical Freundlich constant; 1/n, Freundlich heterogeneity parameter; qmax, fitted Langmuir capacity; b, Langmuir affinity constant; A, Temkin constant.

Equilibrium removal of Pb^{2+} and Cd^{2+} was evaluated at 25 °C (Fig. 8 and Table 3) to compare the usable uptake range of the two humic fractions. Freundlich, Langmuir, and Temkin models all produced R^2 values above 0.95; Freundlich fits exceeded 0.98 for both metals and fractions, and fitted 1/n values were below 1. At 25 °C, the fitted Langmuir capacities of HA were 8.97 mg g^{-1} for Pb^{2+} and 6.47 mg g^{-1} for Cd^{2+}. These values support HA as the stronger candidate in a screening comparison, while remaining empirical descriptors that do not validate a treatment configuration or predict performance in multicomponent water.

The Freundlich constant Kf was used only for comparison under identical

conditions. HA had higher fitted Kf values than HM for both metals (Table 3). The difference is consistent with greater apparent accessibility of binding environments in HA, despite HM having the higher bulk oxygen content. These data do not resolve the number, identity or intrinsic affinity of individual sites.

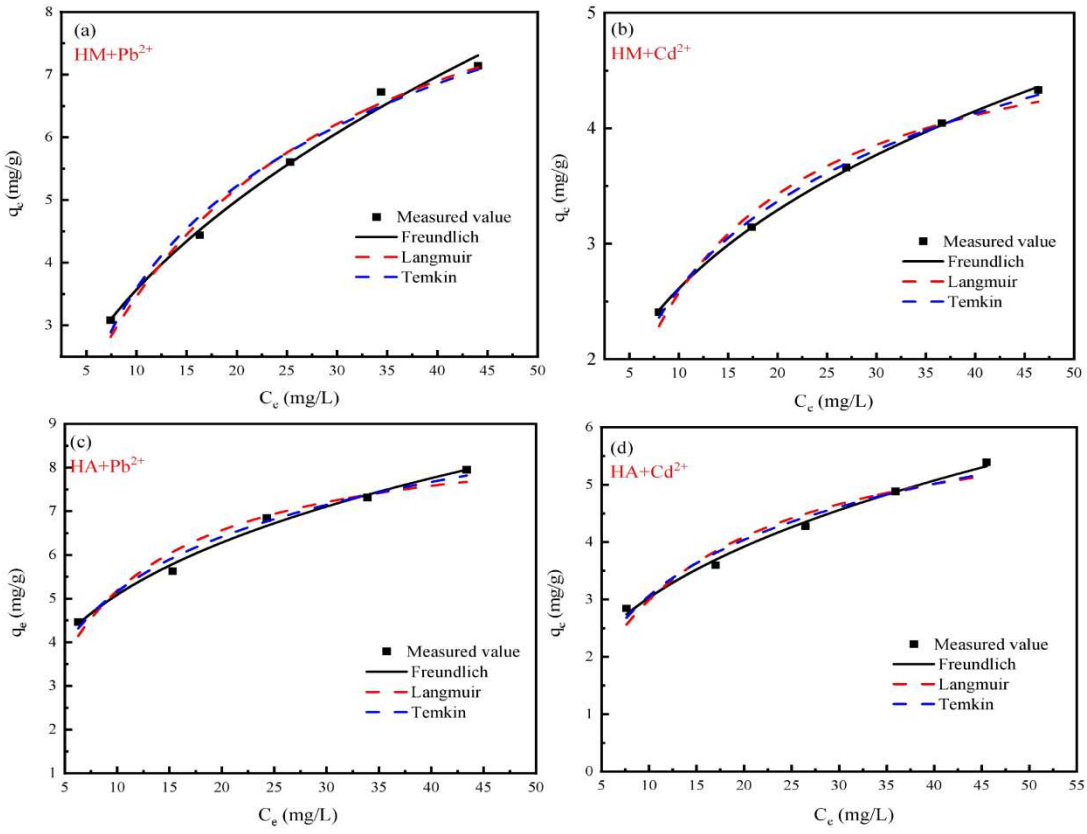


Fig. 8. Isotherm-model comparison for apparent Pb^{2+} and Cd^{2+} uptake by HM and HA: (a) Pb^{2+}–HM, (b) Cd^{2+}–HM, (c) Pb^{2+}–HA, and (d) Cd^{2+}–HA. Fits are empirical descriptors for preliminary sorbent comparison.

3.2.3. pH window for apparent aqueous removal

As illustrated in Fig. 9, operationally defined apparent uptake by HA and HM varied with solution pH. Apparent uptake increased as pH rose. The increase became less pronounced at pH ≥ 5.0 for Cd^{2+} and above approximately pH 3.0 for Pb^{2+}.

At low pH, proton competition and protonation of humic functional groups can reduce metal partitioning to the retained phase. Apparent removal increased as initial

pH rose, consistent with greater deprotonation and electrostatic attraction. No visible precipitate was observed and procedural blanks showed little concentration loss. However, hydrolysis, subvisible precipitation, membrane adsorption and retention of metal-bearing humic colloids cannot be excluded. The response is therefore interpreted as operationally defined apparent removal after 0.45 μm filtration, not adsorption alone. Because final pH was not independently controlled for each batch, these data represent initial-pH conditions rather than rigorously buffered equilibrium states.

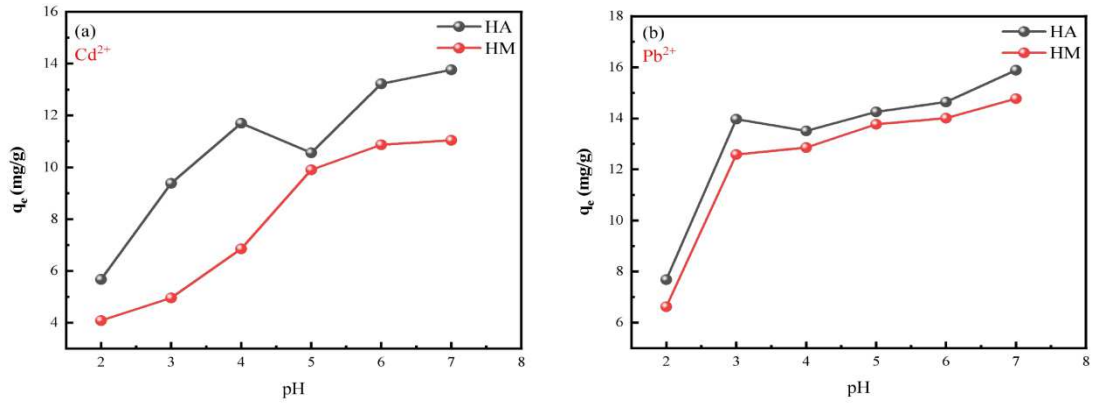


Fig. 9. Effect of initial pH on operationally defined apparent removal of (a) Cd^{2+} and (b) Pb^{2+} by HA and HM after 0.45 μm filtration; the plot defines an initial pH window for screening.

3.3. Material characteristics supporting sorbent selection

3.3.1. Elemental analysis

Table 4 Elemental composition and atomic ratios of HA and HM.

	C%	H%	O%	N%	H/C	O/C	C/N	(O+N)/C	E2/E3	E4/E6
HM	30.27	9.03	57.52	1.88	3.58	1.43	18.82	1.48		

HA	50.41	5.58	40.13	4.38	1.33	0.60	13.46	0.67	2.87	1.83

The elemental composition (C, H, O, N, and S) and corresponding atomic ratios of humic acid (HA) and humin (HM) extracted from the study area are summarized in Table 4. Both HA and HM exhibited comparable elemental profiles, characterized by high proportions of C, H, O, and N and relatively low sulfur (S) contents. HA exhibited a markedly higher carbon content (50.41%) and lower oxygen content (40.13%), whereas HM was characterized by a lower carbon proportion (30.27%) and substantially higher oxygen content (57.52%).

The H/C atomic ratio was 1.33 for HA and 3.58 for HM. Lower H/C values are commonly associated with greater aromaticity and structural unsaturation, whereas higher values indicate more aliphatic character(Olk et al., 2019). C/N ratios were 13.46 for HA and 18.82 for HM, while (O+N)/C ratios were 0.67 and 1.48, respectively. These bulk ratios indicate compositional differences between the fractions, but they do not identify metal coordination geometry or distinguish inner-sphere from outer-sphere binding. The higher total oxygen content of HM also shows that bulk elemental abundance alone cannot explain the stronger apparent uptake by HA.

3.3.2. UV–Vis analysis

The UV–Vis spectrum of HA decreased gradually with increasing wavelength and showed an inflection near 280 nm (Fig. 10), consistent with conjugated aromatic chromophores. HM was not interpreted quantitatively because its low solubility and light scattering prevented measurement under comparable conditions. For HA, E2/E3

and E4/E6 ratios were used as optical proxies for molecular size, aromaticity, and condensation [38,39]. These proxies describe bulk optical characteristics. They do not directly demonstrate electron donation or the stability of metal-specific complexes.

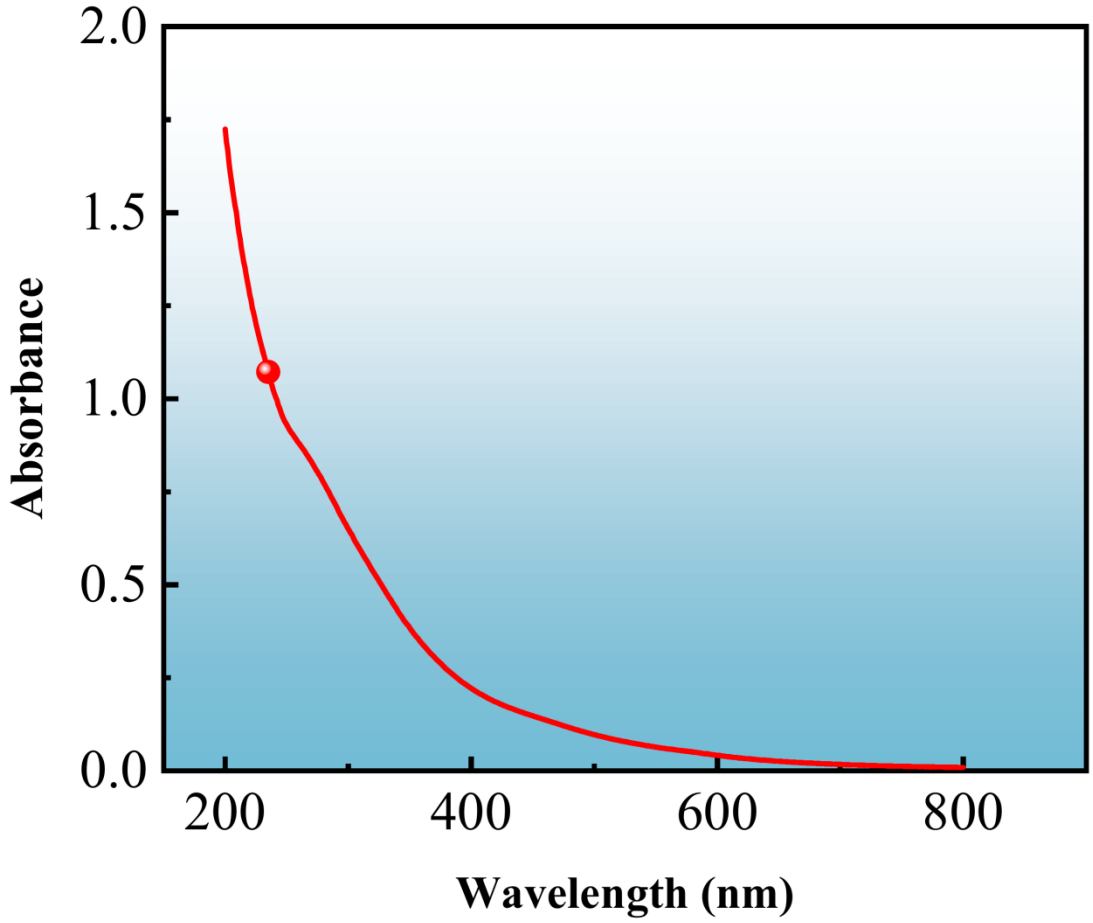


Fig. 10. UV–Vis absorption spectrum of humic acid (HA) over the scanned wavelength range, providing optical context for comparative sorbent selection.

3.3.3. SEM analysis

SEM showed distinct morphologies for HA and HM (Fig. 11). HA had lamellar, sponge-like textures with stacked layers and irregular surfaces, whereas HM formed more compact ovoid aggregates with heterogeneous particle sizes. These images are consistent with differences in the accessibility of external and interparticle sites.

However, SEM does not quantify specific surface area, pore-size distribution, or the density of chemically active sites. The morphological contrast therefore provides supporting context rather than direct evidence for adsorption or complexation mechanisms.

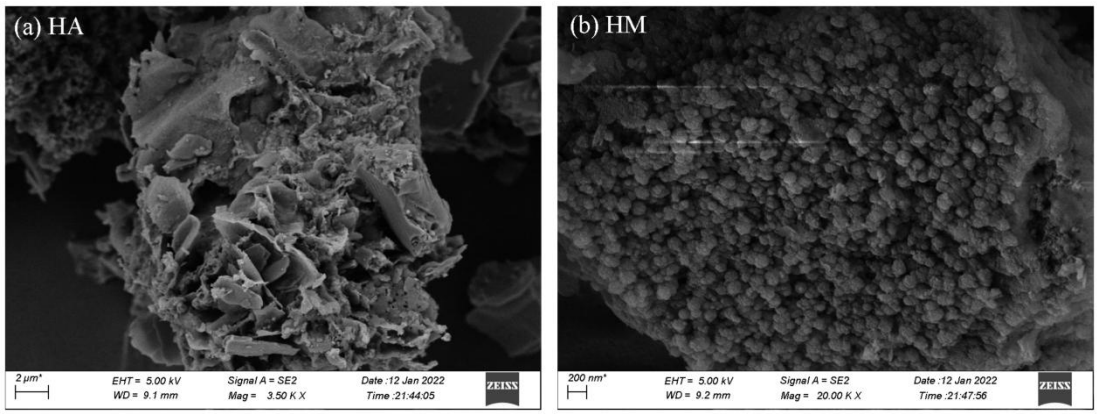


Fig. 11. SEM micrographs of (a) humic acid (HA) and (b) humin (HM), illustrating morphology-related differences that may affect accessibility of sites used in aqueous metal-removal screening.

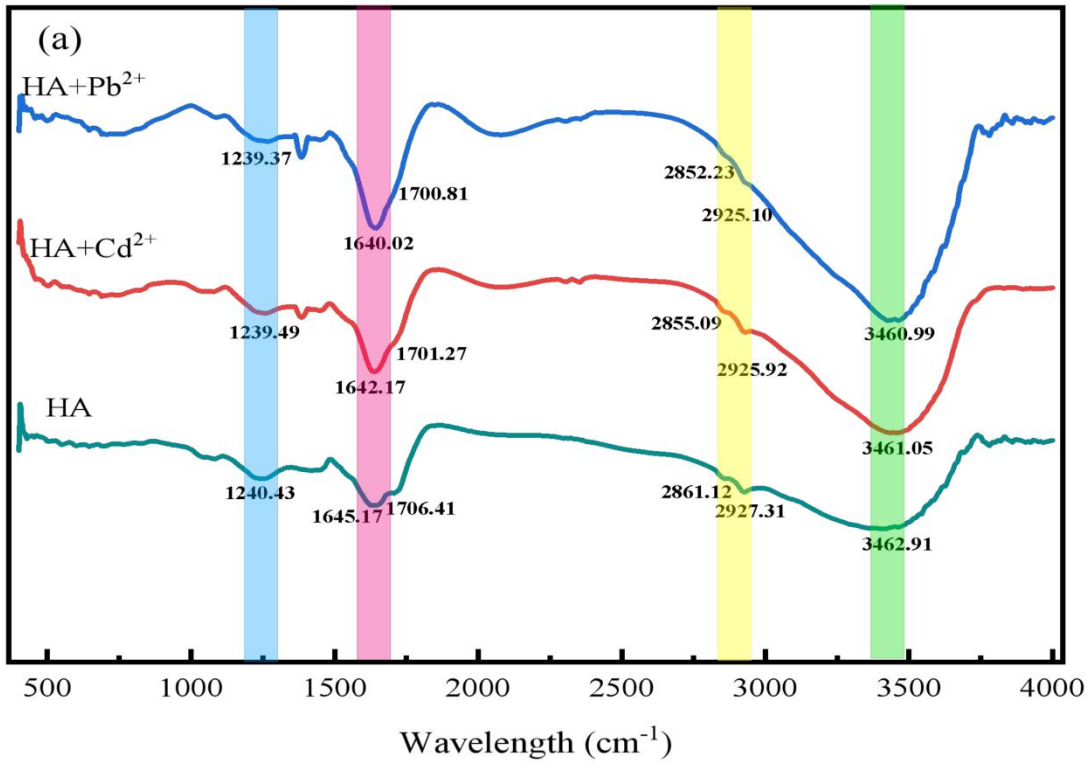
3.3.4. FTIR analysis

FTIR spectra (Fig. 12) were used to identify functional groups and their changes following Pb^{2+} and Cd^{2+} adsorption. Key bands (Table 5) include broad O–H/N–H stretching (3750–3300 cm^{-1}), aliphatic C–H stretching (3000–2700 cm^{-1}), aromatic C=C stretching (1650–1600 cm^{-1}), and C–O/Si–O vibrations (1000–1200 cm^{-1}).

Table 5 Main FTIR bands and tentative assignments.

Wavenumber (cm^{-1})	Chemical Assignment
3750-3300	-OH (carboxylic, phenolic) and -NH stretching vibrations
3030-3080	Aromatic C-H stretching vibrations
3000-2700	Aliphatic C-H stretching vibrations
1710-1722	C=O stretching in amides, quinones, and ketones
1650-1600	Aromatic C=C stretching vibrations
1500-1560	-NH bending and aromatic C=C stretching
1450-1400	Aliphatic C-H bending and aromatic ring vibrations
1240-1200	C=O stretching in $-COO^-$ and -OH deformation
1122-1127	Aliphatic C-O and C-OH stretching
1080-1000	Si-O stretching (silicate impurities) or polysaccharide C-O vibrations
1000-400	C-H bending vibrations

Bands assigned to carboxylate- and phenolic-associated regions shifted to lower wavenumbers after apparent uptake. These changes are consistent with altered bonding environments involving oxygen-containing groups. A band near 1400 cm^{-1} also appeared after treatment and may reflect metal-associated vibrations or structural rearrangement. Because the bands are broad and assignments are not unique, FTIR alone cannot establish coordination geometry or distinguish adsorption from other retention processes.



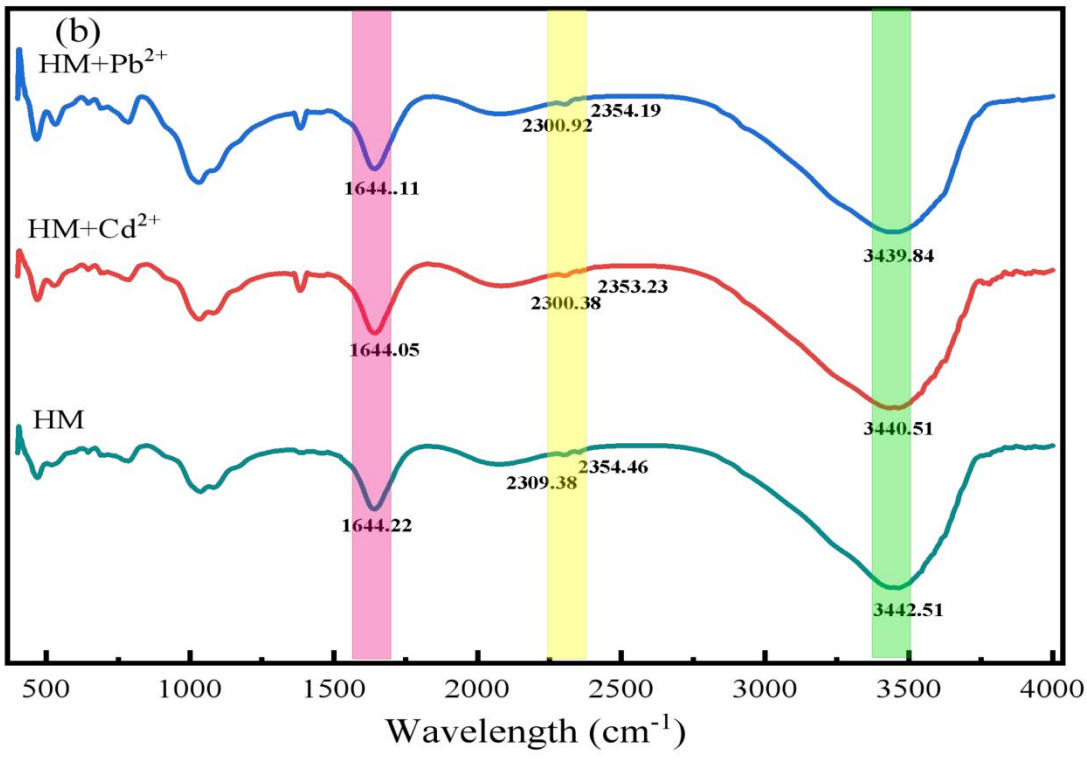


Fig. 12. FTIR spectra of (a) humic acid (HA) and (b) humin (HM) before and after apparent Pb^{2+} and Cd^{2+} uptake, highlighting changes in bands associated with oxygen-containing groups relevant to process interpretation.

3.3.5. Evidence-based process interpretation

Taken together, the characterization data provide a rationale for comparing the two sorbents. The pH response is consistent with greater deprotonation at higher initial pH, while FTIR shifts indicate changes in environments associated with oxygen-containing groups. HA showed faster apparent uptake and higher fitted capacities than HM, and its lamellar morphology is consistent with greater accessibility of some binding environments. These observations support HA for follow-up removal studies, but they do not establish a unique surface-complexation pathway or guarantee performance in real water matrices.

4. Conclusions

This study linked source mobility with preliminary sorbent selection. The lead–zinc slag contained large Pb and Zn inventories and elevated Cd, but standardized acid leaching released Cd at 36.37–44.14 mg L^{-1} while Pb remained below its regulatory limit. Cd was therefore the principal mobile target under the applied conditions, with Pb retained as a high-inventory co-contaminant. Cd/Zn enrichment at W5–W6 and the U2 groundwater anomaly provided receiving-water context, without proving a unique source.

In controlled single-metal batch tests, HA showed faster apparent uptake and higher fitted capacities than HM. At 25 °C, its fitted Langmuir capacities were 8.97 mg g^{-1} for Pb^{2+} and 6.47 mg g^{-1} for Cd^{2+}. Kinetic and isotherm fits supported comparison,

while FTIR shifts were consistent with changes involving oxygen-containing groups. HA is therefore the more promising site-derived fraction for further sorbent development.

The practical implication is a source-to-treatment prioritization workflow. Mobility testing identifies the dissolved-metal target, and batch removal data provide an initial basis for choosing a sorbent and operating window. In this respect, the study complements, rather than replaces, three common research designs: long-term or dynamic leaching studies that resolve source persistence, pretreatment or immobilization studies that alter the source matrix, and real-wastewater adsorption studies that test matrix effects and process performance. The present work addresses the interface between these stages by asking which target and which humic fraction merit those more demanding tests. Apparent removal was measured after 0.45 μm filtration in single-metal nitrate solutions, so adsorption cannot be fully separated from colloid retention, hydrolysis or incipient precipitation. Real leachate or wastewater, competing ions, sorbent recovery, regeneration, hydraulic operation and long-term stability were not evaluated. The study therefore supports treatment development and test prioritization, not a validated treatment technology.

Acknowledgements

The authors gratefully acknowledge the institutional and technical support provided by the College of Agricultural Science and Engineering, Hohai University;

Kunming Engineering Corporation Limited; the School of Environment and Resource, Southwest University of Science and Technology; and the Low-cost Wastewater Treatment Technology International Sci-Tech Cooperation Base of Sichuan Province.

Authors' Contributions

Haiqing Yang: Conceptualization, Investigation, Resources, Writing - original draft. Zhixiao Mao: Conceptualization, Methodology, Formal analysis, Data curation, Supervision, Writing - review and editing. Qiming Wang: Investigation, Validation, Data curation, Visualization, Writing - review and editing. Yong Zhen: Investigation, Resources. Bixia Yuan: Investigation, Validation. Yaoyao Shen: Investigation, Data curation.

Funding

This work was supported by the Key Research and Development Project of China MCC5 Group Corp. Ltd. (Grant No. 2WY2025B001), Yunnan Major Science and Technology Special Project (Grant No. 2202502AE090032), and the Science and Technology Department of Sichuan Province (Grant No. 2024YFNH0001).

Data Availability Statement

The datasets generated and/or analyzed during the current study are available from the corresponding author on reasonable request.

Declarations

Ethical Approval This article does not contain any studies with human participants or

animals performed by any of the authors.

Consent to Participate All the co-authors approved their participation.

Consent to Publish All the co-authors agreed to publish.

Competing Interests The authors declare no competing interests.

References

Chen, D., Li, H., Nan, F., Tan, J., Ma, M., Zhan, W., 2024a. Heavy metals remediation through alkali assisted ball-milling activation of copper smelting slag for resource utilization. J. Environ. Chem. Eng. 12, 113053. https://doi.org/10.1016/j.jece.2024.113053

Chen, D., Tan, J., Li, H., Lin, Y., Nan, F., Han, Q., Zhan, W., 2024b. Integrating a high-energy activation method for the sustainable treatment of iron smelting slag, phosphogypsum, and arsenic-contaminated water. J. Environ. Chem. Eng. 12, 114456. https://doi.org/10.1016/j.jece.2024.114456

Cui, H., Wen, X., Wu, Z., Zhao, Y., Lu, Q., Wei, Z., 2022. Insight into complexation of Cd(II) and Cu(II) to fulvic acid based on feature recognition of PARAFAC combined with 2DCOS. J. Hazard. Mater. 440, 129758. https://doi.org/10.1016/j.jhazmat.2022.129758

Ding, Y., Liu, M., Peng, S., Li, J., Liang, Y., Shi, Z., 2019. Binding characteristics of heavy metals to humic acid before and after fractionation by ferrihydrite. Chemosphere 226, 140–148. https://doi.org/10.1016/j.chemosphere.2019.03.124

Guo, C., Sun, Y., Yang, C., Yang, J., Wang, J., 2026. Interaction of humic acid with heavy metals and its influence on flocculation effect: a review. Water, Air, Soil Pollut. 237, 3–18. https://doi.org/10.1007/s11270-025-08717-1

He, E., Lü, C., He, J., Zhao, B., Wang, J., Zhang, R., Ding, T., 2016. Binding characteristics of Cu2+ to natural humic acid fractions sequentially extracted from the lake sediments. Environ. Sci. Pollut. Res. 23, 22667–22677. https://doi.org/10.1007/s11356-016-7487-2

Hu, S., Xiong, X., Li, X., Wang, M., Xu, D., Zhou, W., 2025. Distribution and leachability of heavy metals from lead-zinc tailings with different degrees of chemical weathering in the qinling mountains. Appl. Geochem. 189, 106434. https://doi.org/10.1016/j.apgeochem.2025.106434

Klučáková, M., Enev, V., 2024. Migration of copper(II) ions in humic systems—effect of incorporated calcium(II), magnesium(II), and iron(III) ions. Environ. Sci. Pollut. Res. 31, 52996–53007. https://doi.org/10.1007/s11356-024-34758-w

Kögel-Knabner, I., 2017. The macromolecular organic composition of plant and microbial residues as inputs to soil organic matter: fourteen years on. Soil Biol. Biochem. 105, A3–A8. https://doi.org/10.1016/j.soilbio.2016.08.011

Lin, Y., Ma, J., Zhang, Z., Zhu, Y., Hou, H., Zhao, L., Sun, Z., Xue, W., Shi, H., 2018. Linkage between human population and trace elements in soils of the pearl river delta: implications for source identification and risk assessment. Sci. Total Environ. 610–611, 944–950. https://doi.org/10.1016/j.scitotenv.2017.08.147

Lu, Q., Wang, Z., Wang, J., Xie, L., Liu, Q., Zeng, H., 2023. Deciphering the specific interaction of humic acid with divalent cations at the nanoscale. Chem. Eng. J. 470, 144097. https://doi.org/10.1016/j.cej.2023.144097

Luo, Y., He, Y., Zhou, D., Pan, L., Wu, Y., 2024. Organic amendment application affects the release behaviour, bioavailability, and speciation of heavy metals in zinc smelting slag: insight into dissolved organic matter. J. Hazard. Mater. 465, 133105. https://doi.org/10.1016/j.jhazmat.2023.133105

Ma, J., Zhou, P., Liu, Y., Lian, W., Feng, B., Li, L., Zhao, Y., Weng, L., Lei, G., Li, H., 2025. Humic acid with vertical adsorption conformation enhanced the transport of petroleum hydrocarbon-contaminated colloids. Environ. Sci. Technol. 59, 4092–4103. https://doi.org/10.1021/acs.est.4c11233

Ma, Y., Li, C., Yan, J., Yu, H., Kan, H., Yu, W., Zhou, X., Meng, Q., Dong, P., 2023. The release analysis of As and Cr metals in lead-zinc smelting slag: mineralogical analysis, bioavailability and leachability analysis. Environ. Res. 229, 115751. https://doi.org/10.1016/j.envres.2023.115751

Moghimi Dehkordi, M., Pournuroz Nodeh, Z., Soleimani Dehkordi, K., Salmanvandi, H., Rasouli Khorjestan, R., Ghaffarzadeh, M., 2024. Soil, air, and water pollution from mining and industrial activities: sources of pollution, environmental impacts, and prevention and control methods. Results Eng. 23, 102729. https://doi.org/10.1016/j.rineng.2024.102729

Mohammadi, A.A., Zarei, A., Esmaeilzadeh, M., Taghavi, M., Yousefi, M., Yousefi, Z., Sedighi, F., Javan, S., 2020. Assessment of heavy metal pollution and human health risks assessment in soils around an industrial zone in neyshabur, iran. Biol. Trace Elem. Res. 195, 343–352. https://doi.org/10.1007/s12011-019-01816-1

Olk, D.C., Bloom, P.R., Perdue, E.M., McKnight, D.M., Chen, Y., Farenhorst, A., Senesi, N., Chin, Y. -P., Schmitt-Koplin, P., Hertkorn, N., Harir, M., 2019. Environmental and agricultural relevance of humic fractions extracted by alkali from soils and natural waters. J. Environ. Qual. 48, 1126–1126. https://doi.org/10.2134/jeq2019.02.0041er

Pan, H., Shi, L., Liu, X., Lei, H., Yang, G., Chen, H., 2023. Interactions between humic acid and the forms and bioavailability of copper in water. Water, Air, Soil Pollut. 234, 312–329. https://doi.org/10.1007/s11270-023-06326-4

Peng, J., Zhang, S., Han, Y., Bate, B., Ke, H., Chen, Y., 2022. Soil heavy metal pollution of industrial legacies in China and health risk assessment. Sci. Total Environ. 816, 151632. https://doi.org/10.1016/j.scitotenv.2021.151632

Piatak, N.M., Parsons, M.B., Seal, R.R., 2015. Characteristics and environmental aspects of slag: a review. Appl. Geochem. 57, 236–266. https://doi.org/10.1016/j.apgeochem.2014.04.009

641 Qu, C., Chen, J., Mortimer, M., Wu, Y., Cai, P., Huang, Q., 2022. Humic acids restrict
642 the transformation and the stabilization of Cd by iron (hydr)oxides. J. Hazard.
643 Mater. 430, 128365. https://doi.org/10.1016/j.jhazmat.2022.128365
644 Rodríguez, L., Ruiz, E., Alonso-Azcárate, J., Rincón, J., 2009. Heavy metal distribution
645 and chemical speciation in tailings and soils around a Pb–Zn mine in Spain. J.
646 Environ. Manage. 90, 1106–1116. https://doi.org/10.1016/j.jenvman.2008.04.007
647 Shu, K., Sasaki, K., 2022. Occurrence of steel converter slag and its high value-added
648 conversion for environmental restoration in China: a review. J. Cleaner Prod. 373,
649 133876. https://doi.org/10.1016/j.jclepro.2022.133876
650 Srinivasa Gowd, S., Ramakrishna Reddy, M., Govil, P.K., 2010. Assessment of heavy
651 metal contamination in soils at jajmau (kanpur) and unnao industrial areas of the
652 ganga plain, uttar pradesh, india. J. Hazard. Mater. 174, 113–121.
653 https://doi.org/10.1016/j.jhazmat.2009.09.024
654 Subdiaga, E., Orsetti, S., Haderlein, S.B., 2019. Effects of sorption on redox properties
655 of natural organic matter. Environ. Sci. Technol. 53, 14319–14328.
656 https://doi.org/10.1021/acs.est.9b04684
657 Tan, L., Yu, Z., Tan, X., Fang, M., Wang, Xiangxue, Wang, J., Xing, J., Ai, Y., Wang,
658 Xiangke, 2019. Systematic studies on the binding of metal ions in aggregates of
659 humic acid: aggregation kinetics, spectroscopic analyses and MD simulations.
660 Environ. Pollut. 246, 999–1007. https://doi.org/10.1016/j.envpol.2019.01.007
661 Tandy, S., Bossart, K., Mueller, R., Ritschel, J., Hauser, L., Schulin, R., Nowack, B.,
662 2004. Extraction of heavy metals from soils using biodegradable chelating agents.
663 Environ. Sci. Technol. 38, 937–944. https://doi.org/10.1021/es0348750
664 Tang, W.-W., Zeng, G.-M., Gong, J.-L., Liang, J., Xu, P., Zhang, C., Huang, B.-B., 2014.
665 Impact of humic/fulvic acid on the removal of heavy metals from aqueous
666 solutions using nanomaterials: a review. Sci. Total Environ. 468–469, 1014–1027.
667 https://doi.org/10.1016/j.scitotenv.2013.09.044
668 Tao, M., Zhang, X., Wang, S., Cao, W., Jiang, Y., 2019. Life cycle assessment on lead–
669 zinc ore mining and beneficiation in China. J. Cleaner Prod. 237, 117833.
670 https://doi.org/10.1016/j.jclepro.2019.117833
671 Thurman, E.M., Malcolm, R.L., 1981. Preparative isolation of aquatic humic
672 substances. Environ. Sci. Technol. 15, 463–466.
673 https://doi.org/10.1021/es00086a012
674 Wang, A., Liu, Y., Zhang, Y., Ren, J., Zeng, Y., Huang, Z., 2024. Synthesis of biochar
675 modified steel slag composites for passivation of multiple heavy metals in soil. J.
676 Environ. Chem. Eng. 12, 114026. https://doi.org/10.1016/j.jece.2024.114026
677 Wang, G., Luo, W., Teng, Z., Zhao, X., Cheng, Y., Wang, Y., Liu, B., Lu, M., Li, M.,
678 2025. Humic and fulvic acid-mediated dissimilatory iron reduction coupled with
679 phosphate solubilizing bacteria inducing secondary mineral formation for efficient
680 cadmium immobilization. J. Hazard. Mater. 496, 139297.
681 https://doi.org/10.1016/j.jhazmat.2025.139297
682 Wang, Z., Lu, Q., Liu, C., Tian, H., Wang, J., Xie, L., Liu, Q., Zeng, H., 2024. Nanoscale

insights into the interaction mechanism underlying the adsorption and retention of heavy metal ions by humic acid. Environ. Sci. Technol. acs.est.3c08309. https://doi.org/10.1021/acs.est.3c08309

Xiong, J., Koopal, L.K., Tan, W., Fang, L., Wang, M., Zhao, W., Liu, F., Zhang, J., Weng, L., 2013. Lead binding to soil fulvic and humic acids: NICA-donnan modeling and XAFS spectroscopy. Environ. Sci. Technol. 47, 11634–11642. https://doi.org/10.1021/es402123v

Xu, D.-M., Fu, R.-B., Tong, Y.-H., Shen, D.-L., Guo, X.-P., 2021. The potential environmental risk implications of heavy metals based on their geochemical and mineralogical characteristics in the size-segregated zinc smelting slags. J. Cleaner Prod. 315, 128199. https://doi.org/10.1016/j.jclepro.2021.128199

Zeng, B., Zhang, Z., Yang, S., Mo, L., Jin, F., 2023. Alkanolamines-activated steel slag for stabilization/solidification of heavy metal contaminated soil. J. Environ. Chem. Eng. 11, 110301. https://doi.org/10.1016/j.jece.2023.110301

Zhou, J., Liu, Z., Li, Z., Xie, R., Jiang, X., Cheng, J., Chen, T., Yang, X., 2025. Heavy metals release in lead-zinc tailings: effects of weathering and acid rain. J. Hazard. Mater. 483, 136645. https://doi.org/10.1016/j.jhazmat.2024.136645

Zhou, L., Xu, X., Wang, Q., Park, J., Han, Y., Guo, L., Chen, R., 2024. Microscopic mechanisms and durability evaluation under freeze-thaw conditions of heavy metal solidification in red mud-slag geopolymer. Journal of Environmental Chemical Engineering 12, 114768. https://doi.org/10.1016/j.jece.2024.114768

Supplementary Files

This is a list of supplementary files associated with this preprint. Click to download.

- SupplementaryInformation.docx